

Article

The Multifrequency Future for Remote Sensing of Sea Surface Salinity from Space

David M. Le Vine ^{1,*}  and Emmanuel P. Dinnat ^{1,2} ¹ Goddard Space Flight Center, Greenbelt, MD 20771, USA; emmanuel.dinnat@nasa.gov² CEESMO, Chapman University, Orange, CA 92866, USA

* Correspondence: david.m.levine@nasa.gov; Tel.: +1-301-614-6540

Received: 13 March 2020; Accepted: 21 April 2020; Published: 27 April 2020



Abstract: Passive microwave remote sensing of sea surface salinity from space is done with measurements in the 27 MHz wide spectral window at 1.413 GHz (L-band) which is protected for passive use only. The frequency, 1.413 GHz, is near the peak in sensitivity to changes in salinity and modern L-band instruments, such as the radiometers on SMOS and Aquarius, have demonstrated the feasibility of monitoring surface salinity from space. They have also demonstrated the need for better accuracy, especially in cold water. Proposals to improve accuracy have largely involved adding more frequencies. For example, adding higher frequencies to improve the correction for sea surface temperature and lower frequencies to improve the sensitivity to salinity in cold water. These strategies involve trade-offs, some obvious such as the effects of interference outside the protected band and loss of spatial resolution at lower frequencies, but some are more subtle because of the interdependence of the measurement on other parameters of the ocean surface, in particular, the interdependence of salinity, water temperature and roughness (wind speed). The objective of this manuscript is to describe these interdependencies in a quantitative way with documented assumptions to support the design of future instruments for remote sensing of salinity.

Keywords: microwave remote sensing; L-band; ocean remote sensing; sea surface salinity

1. Introduction

1.1. Passive Microwave Remote Sensing Frequencies

Passive microwave remote sensing of the ocean surface from space is done at a small set of frequencies selected for a combination of protection from radio frequency interference (RFI) and sensitivity to parameters of importance. This is illustrated in Figure 1 [1] which lists the frequencies used in contemporary passive remote sensing of the ocean surface. For example, the spectral window at 1.413 GHz is near the peak in sensitivity to sea surface salinity (SSS) and protected for passive use only, and a frequency near 6.9 GHz is close to the peak in response to sea surface temperature (SST). However, algorithms to retrieve these parameters generally employ more than one frequency. The solid circles in Figure 1 indicate the primary frequency (best sensitivity to the parameter desired) and the open circles indicate other frequencies employed in the retrieval algorithms to help correct for competing effects such as attenuation by the atmosphere or the role of surface roughness (wind driven waves) on emission. An exception is remote sensing of SSS which has only employed measurements in the window at 1.413 GHz [2]. However, the demand for better retrieval accuracy, especially in cold water, is driving change. Systems are being investigated with lower frequencies to improve sensitivity and with higher frequencies to reduce dependence on ancillary data needed for SST and wind speed [3–5]. The goal of the work presented here is to provide information to guide in the choice of additional frequencies for a future generation of instruments to retrieve SSS from space.

	Frequency (GHz)					
	1.4	6.9	10.7	18.7	23.8	37
Protection	Yes	Shared	Yes	Shared	Yes	Shared
Bandwidth (protected)	27		20		200	
Applications						
Sea Surface Salinity	•					
Sea Surface Temperature		•	○	○	○	○
Wind Speed		○	•	○	○	○
Sensors (Bandwidth MHz)						
SMOS/Aquarius/SMAP	27					
AMSR-2		150	100	200	400	1000
Windsat		125	200	750	500	2000

Figure 1. Frequency and bandwidth used by passive microwave sensors in space. The solid circles indicate the primary frequency (best sensitivity to the identified parameter desired) and the open circles indicate other frequencies employed in the retrieval algorithms to help correct for competing effects on observed emissivity.

1.2. Remote Sensing of Sea Surface Salinity

Salinity of ocean water is important to understand ocean circulation and the associated movement of heat and to help understand the global hydrological cycle (e.g., the balance between evaporation and precipitation). Sensors such as on the Soil Moisture and Ocean Salinity (SMOS) mission [6], deployed by the European Space Agency (ESA), and Aquarius [7] and on the Soil Moisture Active Passive (SMAP) mission [8], deployed by the National Aeronautics and Space Administration (NASA), have demonstrated the feasibility of measuring SSS from space (e.g., [9,10]). However, while these L-band radiometers have demonstrated the feasibility of monitoring salinity, they have also demonstrated the need for better accuracy, especially at high latitude and cold water [9,11–14]. These areas are dynamic with high wind and melting ice and the location of turning points in ocean circulation [15,16], all of which are of increasing importance in understanding the consequences of climate change. While winds (roughness) and changing sea ice contribute to error, the substantial decrease in radiometric sensitivity to salinity in cold water is an important part of the increase in Root Mean Square (RMS) error observed in the retrieved salinity.

The radiometers on SMOS, SMAP and Aquarius all operate in a narrow, 27 MHz wide, spectral window at 1.413 GHz protected for passive use only (Appendix D). Proposals to improve accuracy have largely involved adding more frequencies (e.g., measurements near 3–6 GHz to improve the correction for SST) and moving to lower frequencies to improve the sensitivity to salinity in cold water. Examples are instrument studies recently reported at NASA’s Jet Propulsion Laboratory [3] and Goddard Space Flight Center [4,5]. These strategies involve trade-offs, some obvious such as the potential increase in RFI when moving out of the protected band and the poorer spatial resolution that likely comes with lower frequencies, but some are more subtle. More subtle issues arise because of the dependence of the remote sensing measurement on other parameters of the surface, a dependence which must be included in the retrieval algorithm. An example is SST, which in current algorithms to retrieve salinity is obtained as ancillary data from other sources [17]. As will be shown below, moving to a lower frequency to improve sensitivity to salinity also slightly decreases the sensitivity to roughness (a source of uncertainty) but can dramatically increase the sensitivity to SST. Increased sensitivity to SST also increases the sensitivity of the retrieval to error in the ancillary data available to provide SST.

2. Methods

This manuscript will examine the changes in sensitivity of radiometric brightness temperature (TB) to SSS, SST and wind speed (WS) in the context of future instruments for remote sensing of SSS that may operate outside the protected spectral band at 1.413 GHz. To a first approximation, one could represent the change of TB (SSS, SST, WS) in the form:

$$\Delta TB = dTB/dSSS \Delta SSS + dTB/dSST \Delta SST + dTB/dWS \Delta WS \quad (1)$$

The objective of the discussion below is to examine each of the derivative terms in this expansion to provide insight into how the three sensitivities depend on frequency and on the parameters SSS, SST and WS themselves. From the perspective of remote sensing of salinity, one would like to operate in a regime where the sensitivity, $dTB/dSSS$, is large and the other terms are small. The goal of the analysis below is to present quantitative estimates based on documented assumptions about how these terms change to provide the insight needed to optimize choices and to better support the design of a future instrument to measure SSS.

This manuscript consists of several parts which taken together will build a documented description of the response of the ocean surface to SSS, SST and WS. In Section 3.1, the sensitivity of TB to changes in salinity will be discussed (e.g., as a function of frequency, polarization and temperature). In Section 3.2, the sensitivity of TB to changes in SST will be discussed as a function of SSS, temperature and polarization and incidence angle. Both of these sections will assume a flat surface (no sea surface roughness). In Section 3.3, the effect of roughness and the sensitivity of TB to changes in roughness (wind speed, WS) will be discussed, using a combination of theory and empirical model. Finally, in Section 4, this information will be put together to create a figure summarizing these effects and to provide insight into the potential choice of new frequencies to improve accuracy of SSS in future remote sensing instruments.

The figures in Section 4 are a modern and documented version of a figure that has been used to explain the rationale behind the choice of frequencies employed in passive microwave remote sensing of the ocean surface. The original figure [18] is more notional than quantitative and did not have a scale for sensitivity nor mention differences in polarization. One objective of this manuscript is to present an alternative, with appropriate background and detail that will be more useful for this purpose in the future.

3. Results

3.1. Sensitivity of Brightness Temperature (TB) to Changes in Salinity: $dTB/dSSS$

This section reports the sensitivity of the observable, TB, to changes in the ocean variable of primary interest, SSS: $dTB/dSSS$. The sensitivity is strongly dependent on frequency, water temperature and incidence angle. This is illustrated below in Figures 2–5.

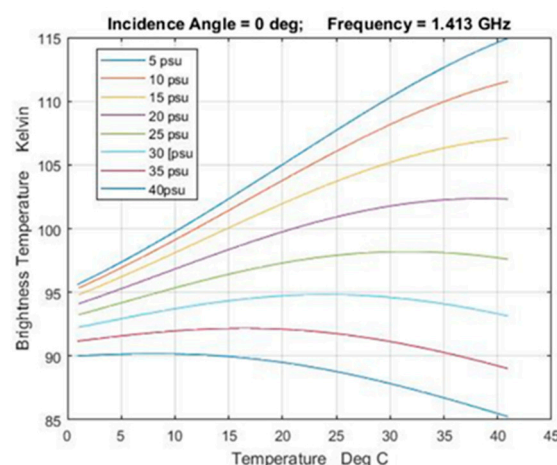


Figure 2. Brightness temperature as a function of SST for constant SSS. The calculations are for a flat surface (no wind), a frequency of 1.413 GHz and at nadir (zero incidence angle). The calculations use the Klein-Swift dielectric constant model function [19].

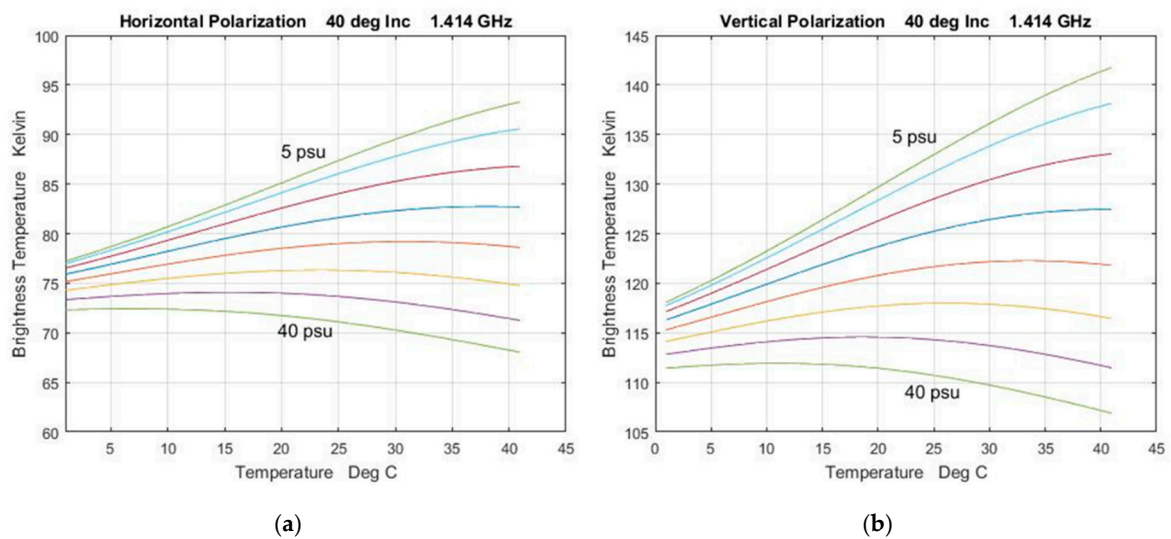


Figure 3. Brightness temperature as a function of SST for constant SSS. The calculations are for a flat surface (no wind) with a frequency of 1.413 GHz and 40° incidence angle. Horizontal polarization (a); Vertical polarization (b). The calculations use the Klein-Swift dielectric constant model function [19].

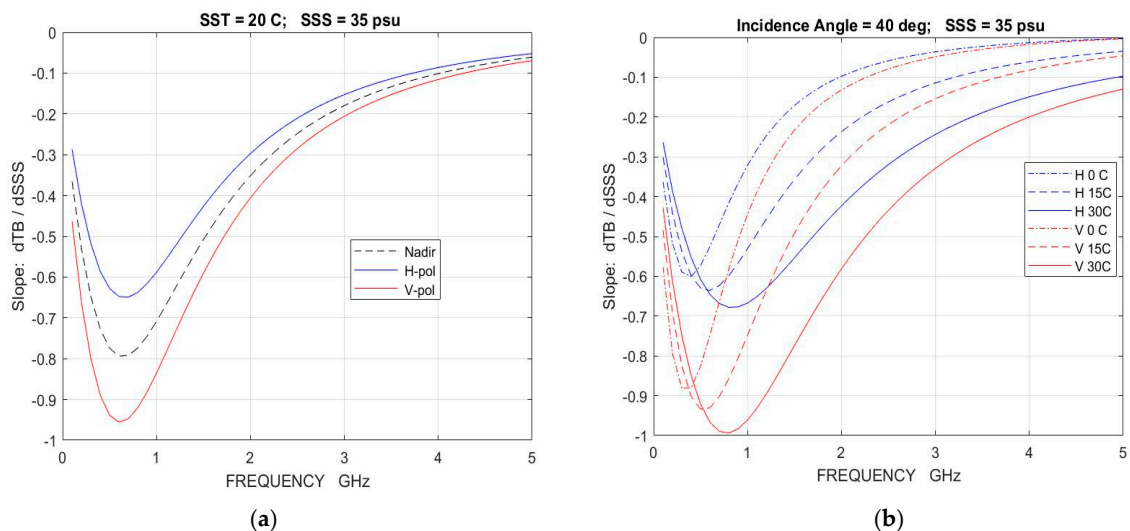


Figure 4. Sensitivity of brightness temperature, TB, to changes in salinity, SSS, as a function of frequency: (a) dependence on incidence angle (SST = 20 °C; SSS = 35 psu); (b) dependence on SST at 40° incidence angle (SSS = 35 psu). These results are for a flat surface (no roughness) and use the Klein-Swift [19] model function for the dielectric constant of sea water. Above 5 GHz, the curves continue the reported trend and converge to 0.

The dependence on water temperature is illustrated in Figure 2 which is a set of level curves of constant salinity as a function of brightness temperature (vertical axis) and water temperature (horizontal axis). The top curve is for SSS = 5 psu and the salinity increases in steps of 5 psu toward the bottom-most curve at SSS = 40 psu. Typical values of SSS in the open ocean are between 33 and 36 psu. The sensitivity of TB to changes in salinity at fixed temperature is approximately the vertical distance between curves in kelvin divided by the difference in salinity.

The sensitivity of TB to SSS is negative (i.e., the brightness temperature decreases as the salinity increases) for all temperatures and salinities in the ocean. The sensitivity also depends on polarization. This is illustrated in Figure 3 which shows the same data at 40° incidence angle for horizontal polarization (Figure 3a) and vertical polarization (Figure 3b). The shape of the curves and dependence

on salinity is similar, but the distance between curves is larger at vertical polarization (easily noticeable at warm temperatures).

The sensitivity itself, $dTB/dSSS$, is shown in Figure 4 as a function of frequency. Figure 4a also illustrates the dependence on incidence angle, and Figure 4b illustrates how the sensitivity varies with temperature. It is clear from the two examples in Figure 4 that the sensitivity depends on incidence angle and temperature and, for incidence angles other than nadir, that sensitivity depends on polarization and is larger at vertical polarization. It is also clear from Figure 4 that the sensitivity is small except for a relatively narrow range of frequencies from about 300 MHz to 3.0 GHz and peaks between 500 MHz and 1 GHz, depending on SST.

3.1.1. Background

The curves in Figures 2–4 were generated using the Klein-Swift model function for the dielectric constant of seawater [19] evaluated at 1.413 GHz, the center frequency of the band in which the measurements from space are currently being made. Assuming a flat surface (no waves) and a homogeneous ocean in thermal equilibrium, one can show [20] that the emissivity of the surface is:

$$\epsilon = 1 - |R_p|^2 \quad (2)$$

where R_p is the Fresnel reflection coefficient at polarization, p :

$$R_v = \frac{\epsilon \cos \theta - \sqrt{\epsilon - \sin^2 \theta}}{\epsilon \cos \theta + \sqrt{\epsilon - \sin^2 \theta}} \quad (3a)$$

$$R_h = \frac{\cos \theta - \sqrt{\epsilon - \sin^2 \theta}}{\cos \theta + \sqrt{\epsilon - \sin^2 \theta}} \quad (3b)$$

and by definition (of microwave emissivity) the brightness temperature, $TB = \epsilon \times T$ where T is the physical temperature. In Equation (3) for the reflection coefficient, ϵ is the dielectric constant of sea water, θ is the local incidence angle and $[h,v]$ indicate polarization (horizontal, vertical, respectively). There has been recent work on the model function, $\epsilon(S,T)$, that gives the dielectric constant of seawater as a function of salinity, S , and physical temperature, T . For example, Meissner and Wentz [21,22] made adjustments based on observations at higher frequencies; and Zhou et al. [23] produced a new model function based on extensive measurements at 1.413 GHz [24]. However, the Klein-Swift model function [19] is still widely used and the difference in the context of the discussion presented here is not significant (Appendix A).

3.1.2. Dependence of Sensitivity, $dTB/dSSS$, on Temperature

The sensitivity to salinity, $dTB/dSSS$, is strongly dependent on water temperature, SST, as shown in Figure 4b. Figure 4b shows the sensitivity at 40° incidence and $SSS = 35$ psu for several temperatures: $SST = 0^\circ C, 15^\circ C, 30^\circ C$. The red curves are for vertical polarization and the blue curves for horizontal polarization. Two changes occur with a change in temperature: as temperature decreases, the peak value decreases and moves toward lower frequency. In addition, the frequency range where the sensitivity is largest (i.e., the width of the peak) becomes narrower with decreasing temperature. This makes the effect of temperature for a sensor operating at a fixed frequency more significant. For example, at 1.4 GHz (currently used by SMOS and SMAP to monitor salinity), the sensitivity $dTB/dSSS$ dramatically decreases with decreasing temperature. Using 1.5 GHz as an example, the change at vertical polarization would be from a sensitivity of about -0.8 K/psu at $SST = 30^\circ C$ to about -0.25 K/psu at $SST = 0^\circ C$. This is representative of the difference in sensitivity between measurements of SSS made at low latitude in the open ocean (warm water) and those made near melting ice in the Arctic.

3.1.3. Dependence of $dTB/dSSS$ on Salinity

At 1.4 GHz there is also a dependence of the sensitivity, $dTB/dSSS$, on salinity, but this is mostly important only at low values of salinity well outside the range of values common in the open ocean. This is illustrated in Figure 5. Figure 5a shows the sensitivity, $dTB/dSSS$, on the vertical axis as a function of salinity on the horizontal axis for several values of SST (at nadir and 1.413 GHz). Figure 5b is a histogram showing the distribution of SSS in the open ocean. The ocean data were taken from in situ measurements made by the global network of Argo floats [25]. Figure 5b shows that the vast majority of measurements are between 33 and 37 psu and from Figure 5a one sees that the sensitivity of brightness temperature to changes in SSS varies relatively little with SSS in this range. Lower salinity can occur in the very cold waters of the Arctic ocean, but even in these regions of extremely fresh ocean waters, SSS is above 25 psu where (Figure 5a) there is limited change in sensitivity with SSS.

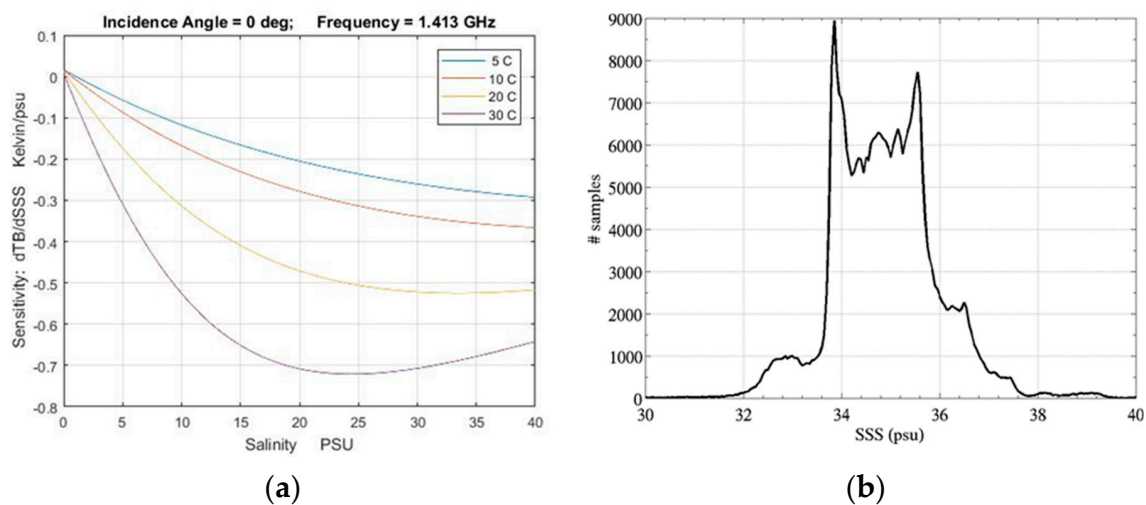


Figure 5. (a) Sensitivity of change in brightness temperature to a change in salinity, $dTB/dSSS$, as a function of salinity for several temperatures. This curve is for 1.413 GHz at normal incidence and no roughness. Based on the Klein-Swift [19] model function; (b) Histogram of number of samples for each salinity reported by Argo floats near Aquarius footprints for the period 2011–2015.

However, the dependence of the sensitivity, $dTB/dSSS$, on salinity is dependent on frequency. In particular, the dependence of the sensitivity on SSS is stronger near the peak of $dTB/dSSS$ (e.g., near 700 MHz in Figure 4a) than on the shoulders as described above for 1.4 GHz. In fact, 1.4 GHz is near a null in the dependence of $dTB/dSSS$ on salinity. This is illustrated in Appendix B where an example (Figure A4) is presented showing the dependence of $dTB/dSSS$ on SSS as a function of frequency for SST = 25 °C.

3.2. Sensitivity of TB to Changes in Temperature: $dTB/dSST$

This section reports the dependence on frequency, temperature, salinity and polarization of the sensitivity of brightness temperature, TB, to changes in ocean water temperature: $dTB/dSST$. As in the preceding section, the analysis is for a flat surface and an ocean with uniform SST and SSS (i.e., Equation (3) applies) and using the model of Klein-Swift [19] for the dielectric constant of sea water.

The sensitivity of brightness temperature to changes in SST is reported as a function of frequency and incidence angle in Figure 6 and as a function of frequency and SST in Figure 7. Figure 6 shows the sensitivity, $dTB/dSST$, at nadir (dashed) and at 40° incidence angle for horizontal polarization (red) and vertical polarization (green). An angle of 40° was chosen because it is SMAP's incidence angle and close to Aquarius' middle beam's incidence angle. The example in Figure 6 is for SST = 25 °C and, although it is representative of the effect of incidence angle, there is a strong dependence on SST. This is illustrated in Figure 7 which shows the dependence on SST as a function of frequency at nadir.

Figures 6b and 7b are the same data as Figures 6a and 7a, respectively, but with expanded scale to show better the behavior below 20 GHz.

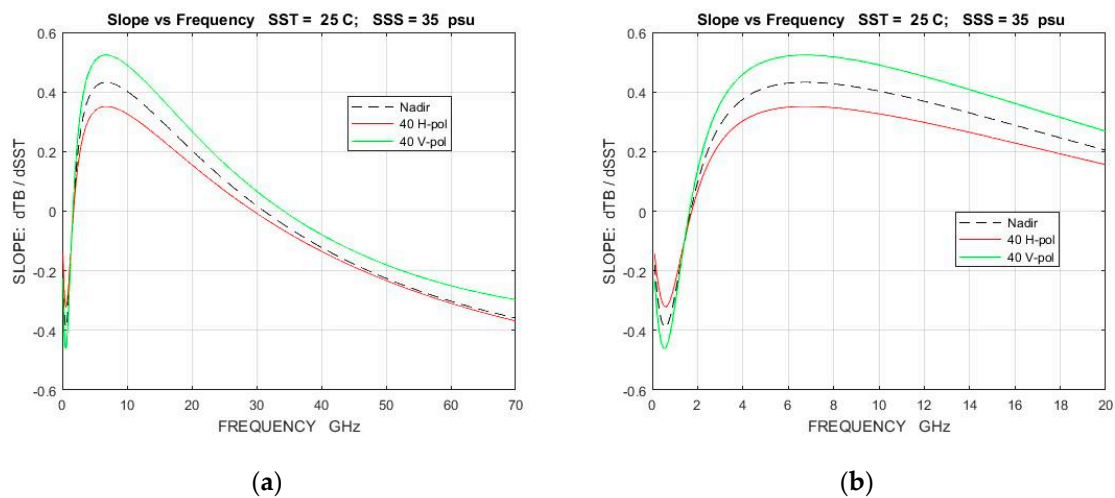


Figure 6. Sensitivity of brightness temperature to changes in temperature, SST, as a function of frequency for SSS = 35 psu and SST = 25 °C. Dashed line at nadir and solid line at 40° incidence angle. These figures are for a flat surface and use the Klein-Swift [19] model function. (b) is the same as (a) with expanded frequency scale to show the behavior at low frequency.

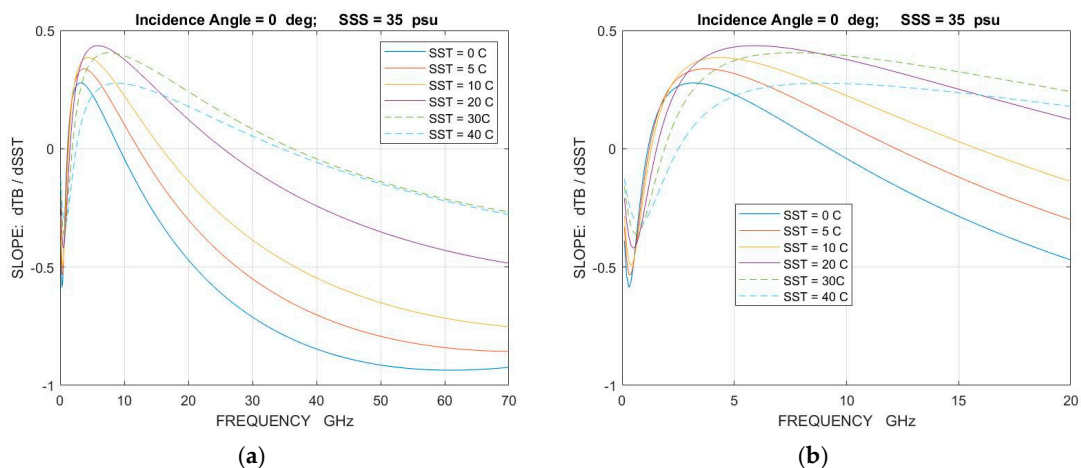


Figure 7. Sensitivity of brightness temperature to changes in temperature, SST, as a function of frequency for selected temperature, at nadir. These curves are for SSS = 35 psu, a flat surface, and use the Klein-Swift [19] model function. (b) is the same as (a) but with expanded frequency scale to show detail below 20 GHz.

Figure 6 illustrates the general trends of $dTB/dSST$ with frequency. The sensitivity changes rapidly with frequency below 10 GHz, with a positive peak near 6 GHz and a negative peak near 600 MHz. The sensitivity passes through zero twice, once near 2 GHz and again in the range near 30 GHz, which varies widely with temperature. The negative peak in sensitivity near 600 MHz is about the same magnitude as the positive peak near 6 GHz. After this positive peak, the sensitivity decreases, crosses zero near 30 GHz and then begins to increase in magnitude again (but negative in sign), eventually reaching a magnitude similar to that at the lower frequency peaks.

The curves in Figure 6 explain the common choice of 6–7 GHz as the primary frequency to measure SST (Figure 1), because in this frequency range the sensitivity to SST is close to the maximum over a wide range of temperatures (Figure 7) and SSS has a very small impact (Figure 4). At low frequency (e.g., below 6 GHz) the sensitivity shown in Figure 7 depends on salinity. However, the change in

sensitivity is small at values of SSS representative of the open ocean (e.g., 32 psu < SSS < 37 psu). An example of the dependence of $dTB/dSST$ on salinity is given in Figure A3 in Appendix B.

The examples of $dTB/dSST$ shown in Figure 6 are for a single temperature, $SST = 25^\circ\text{C}$. However, the sensitivity, $dTB/dSST$, has a strong dependence on SST at all frequencies. This is illustrated in Figure 7 which shows the sensitivity at nadir as a function of SST and frequency. As temperature decreases, the sensitivity curves compress, becoming narrower in frequency and with larger amplitude at the low frequency peak (Figure 7b near 1 GHz) and smaller amplitude at the positive peak. For example, at 5°C the low frequency negative peak is about $-0.5\text{ K}/^\circ\text{C}$ and the positive peak is about $0.3\text{ K}/^\circ\text{C}$ and occurs at about 3 GHz. However, at 30°C the low frequency negative peak is about $-0.4\text{ K}/^\circ\text{C}$ and the positive peak is about $+0.4\text{ K}/^\circ\text{C}$ and occurs near 8 GHz.

The rapid change in $dTB/dSST$ in the frequency range 300 MHz–3.0 GHz is an important consideration for remote sensing of salinity. The frequency of 1.4 GHz where measurements of SSS are currently made (e.g., SMOS and SMAP) is very near the zero of $dTB/dSST$ for water temperature in the range $15\text{--}20^\circ\text{C}$. This can be seen in Figure 7b and also in the level curves of Figures 2 and 3 which are relatively flat for values of salinity representative of the open ocean (e.g., 33–37 psu) and for temperatures in the range $15\text{--}30^\circ\text{C}$. However, moving away from 1.413 GHz in the direction of either higher or lower frequency could significantly increase the magnitude of $dTB/dSST$ and impose a requirement for more accurate information on water temperature in the retrieval algorithm (i.e., require a smaller ΔSST in Equation (1) to compensate for a larger $dTB/dSST$). This could especially be a problem in cold water, where moving to a lower frequency to improve sensitivity to salinity (Figure 4) would also incur an increase in the sensitivity to SST.

3.3. Sensitivity of TB to Wind Speed (WS): dTB/dWS

3.3.1. Background

The radiometric response of the ocean surface in the presence of waves and the relationship of waves to wind is complex and only incompletely modelled. Theories for scattering from the surface suffer from an incomplete description of the surface and the need to integrate over the full range of incidence angles and the entire field-of-view to obtain the radiometric response [20]. Experiments have been made to measure the radiometric response of rough water surfaces (e.g., [22,26–28]) but the experiments are limited to selected frequencies and/or incidence angles and tend to have large error bars, although they do reveal the general behavior with polarization, incidence angle and frequency.

For purposes of this study, the empirical model developed by Meissner and Wentz [22] is used to model the emissivity as a function of wind speed for frequencies above 6 GHz, and a two-scale scattering model developed for SMOS by Yin et al. [29] is used for frequencies below 6 GHz. The empirical model [22] was chosen because it is based on radiometric measurements, covers a large range of frequencies (6–90 GHz), and because it appears to agree reasonably well with available observations ([22] Section 7). This model will be used at the frequencies to which it is matched to the data (6.9, 10.7, 18.7, 37 and 85 GHz) to provide insight into the behavior with incidence angle and SST as a function of frequency. The two-scale model [29] is a physical optics model assuming tilted planes (tilted in two dimensions) with small scale roughness (Bragg scatter) superimposed on each planar facet and modified to include foam. The Yin et al. model agrees well with data from Aquarius, SMOS and SMAP at 1.4 GHz [30]. It will be used for frequencies below 6 GHz and for the examples at 1.4 GHz in Figure 8, Figures 10 and 11.

In both models, the effect of roughness is included explicitly by expressing the emissivity as the sum of two parts:

$$\epsilon = \epsilon_0 + \Delta\epsilon \quad (4)$$

where ϵ_0 is the flat-surface emissivity given by Equations (2) and (3) and $\Delta\epsilon$ is the addition due to wind driven roughness. The wind-dependent correction, $\Delta\epsilon$, used here is taken from Equations (14)–(18) in [22] for frequencies above 6 GHz. The dependence on wind direction has not been included here. For frequency below 6 GHz, the wind-dependent correction is taken from the two-scale model reported

by Yin et al. [29]. At L-band (1.4 GHz) and wind speed below about 15–20 m/s, it agrees well with the empirical correction for wind speed (i.e., geophysical model function) developed from Aquarius and SMAP data [29,31]. Foam is included in the Yin et al. [29] model, and the total emissivity, ϵ_t , is computed from the weighted sum of the rough surface emissivity and the foam emissivity as

$$\epsilon_t = Fr \times \epsilon_f + (1 - Fr) \times \epsilon \quad (5)$$

where Fr is the foam fraction, ϵ_f is the foam emissivity and ϵ is the rough surface emissivity computed from Equation (4).

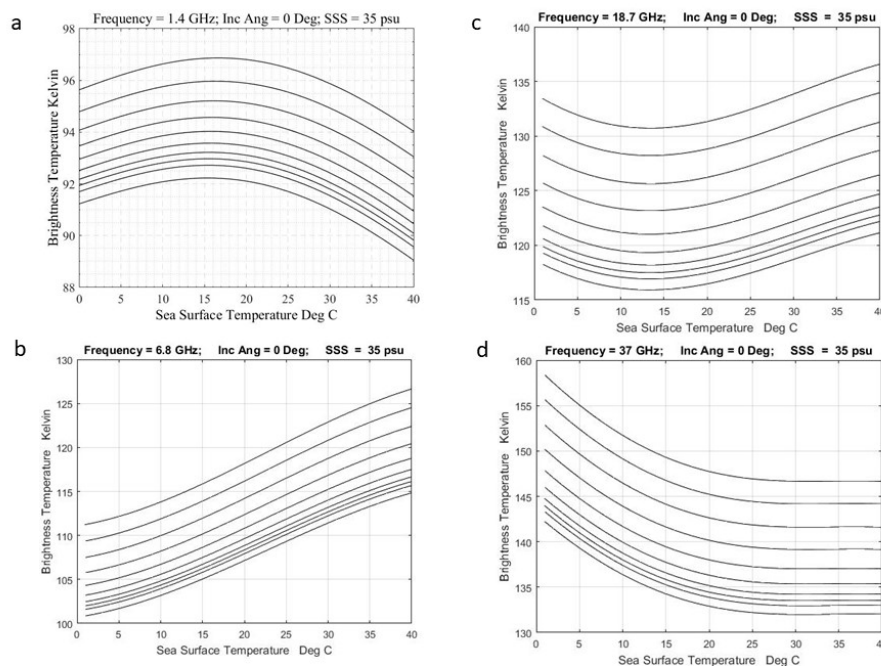


Figure 8. Level curves of TB vs. SST for constant wind speed, WS. The WS increases in steps of 2 m/s starting as zero at the bottom and increasing to 18 m/s at the top. These curves are for nadir (zero incidence angle) and SSS = 35 psu: (a) 1.4 GHz; (b) 6.8 GHz; (c) 18.7 GHz; (d) 37.0 GHz.

3.3.2. Dependence of TB on WS

In general, roughness and foam increase emission (i.e., brightness temperature), and both increase with wind speed. Hence, in general, as wind speed increases, TB also increases, but the sensitivity of TB to wind speed depends on frequency, incidence angle and polarization, being larger for horizontal polarization. These general characteristics are discussed in more detail in the paragraphs below.

The increase of TB as a function of wind speed is illustrated in Figure 8 for frequencies of 1.4 GHz, 6.8 GHz, 18.7 GHz and 37 GHz. Figure 8 is a set of level curves of constant wind speed plotted as a function of brightness temperature on the vertical axis and SST on the horizontal axis. The curves are for zero incidence angle (nadir) and a salinity of 35 psu. The salinity, 35 psu, is typical of the open ocean (Figure 5b), although with the exception of 1.4 GHz the dependence on salinity is negligible (Figure 4). Each curve in Figure 8 represents a constant wind speed, starting at $WS = 0$ m/s at the bottom and increasing in steps of 2 m/s up to 18 m/s for the top curve. At all frequencies there is a monotonic increase in brightness temperature with increasing wind speed. Furthermore, the increase is greater at high wind speed (top curves) than at low wind speed (bottom curves). The transition occurs near a wind speed of 8 m/s.

The shape of the curves as a function of SST is different for each frequency. However, for a fixed frequency the shape is stable and relatively independent of WS (i.e., the level curves in each example in Figure 8 are roughly parallel). The general shape of the curves depends on the bulk properties of

water and is not a wind driven feature. This can be seen by comparing the shape when $WS > 0$ m/s with the lowest curve for which $WS = 0$ m/s. The curve for $WS = 0$ m/s is determined, by definition in Equation (4), by ϵ_0 (i.e., $TB = \epsilon_0 \times T$ when $WS = 0$ m/s). In turn, ϵ_0 is determined by the Fresnel reflection coefficients of a flat surface (i.e., Equations (2) and (3)) and is strongly dependent on both frequency and water temperature (Section 3.2 above). This is further illustrated in Figure 9a which shows brightness temperature, TB , at nadir as function of frequency for $WS = 0$ m/s and for temperatures of 1 °C, 10 °C, 20 °C and 30 °C. The curves in Figure 8 at $WS = 0$ m/s are essentially vertical cuts through Figure 9a at fixed frequency. For example, at 6.8 GHz it is clear that TB increases as a function of temperature but at 35 GHz and higher, the behavior is reversed and TB decreases with an increase in temperature. This behavior can be seen in the change of slope of the level curves in Figure 8 from positive at 6.8 GHz (Figure 8b) to negative at 37 GHz (Figure 8d).

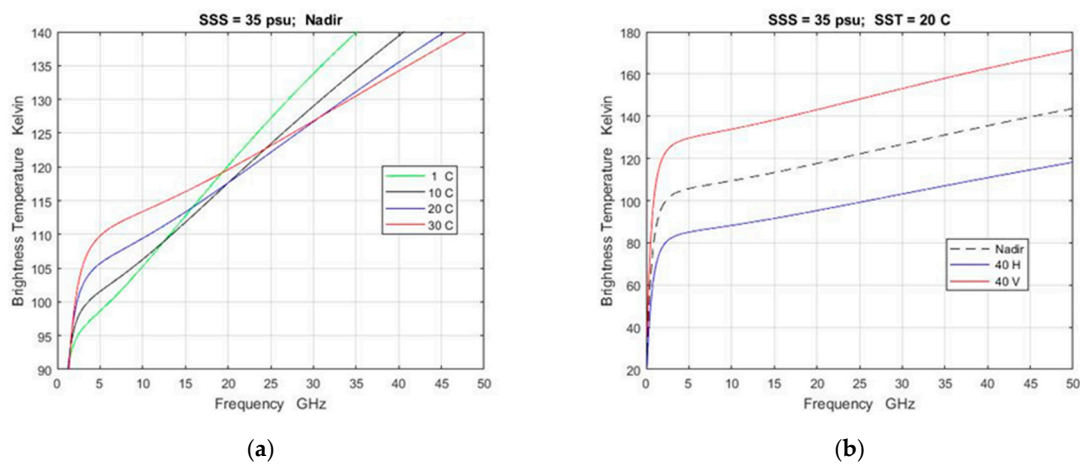


Figure 9. Brightness temperature as a function of frequency: (a) At nadir and several values of SST; (b) SST = 20 °C for nadir and 40° incidence angle. All curves are for SSS = 35 psu, zero wind speed (flat surface) and use the Klein-Swift model function [19] for the dielectric constant of sea water.

Figures 9b and 10 illustrate the behavior with incidence angle and frequency. Figure 9b shows the dependence of TB with frequency at nadir (dashed curve) and 40° incidence angle (red for vertical polarization and blue for horizontal polarization). The dashed curve (nadir) behaves as a function of wind speed and SST as shown in Figure 8 for selected frequencies. Off nadir, horizontal (blue) and vertical (red) polarization behave similarly but with amplitude that depends on polarization. This is illustrated further in Figure 10 which shows brightness temperature as a function of SST at nadir and 40° incidence angle for frequencies, 1.4 GHz (Figure 10a), 6.8 GHz (Figure 10b) and 18.7 GHz (Figure 10c). The red curves are for vertical polarization and the blue curves for horizontal polarization at an incidence angle of 40°. The dashed blue and red curves are for $WS = 0$ m/s and the solid curves for $WS = 7$ m/s and 14 m/s. The dashed black curve is for nadir and $WS = 0$ m/s and is the same as the lowest curve ($WS = 0$ m/s) in Figure 8a–d. The effect of wind speed is to increase the emissivity and brightness temperature at both polarizations. Comparing the shape of the dashed curves in Figure 10 (zero wind speed) shows that the shape (change with SST) is, to a good approximation, independent of incidence angle; however, comparing the spacing between red lines with spacing between blue lines indicates that the sensitivity to WS does vary with polarization. In particular, the distance between the blue curves (horizontal polarization) is greater than between the red curves (vertical polarization) indicating that the sensitivity to WS is greater at horizontal polarization.

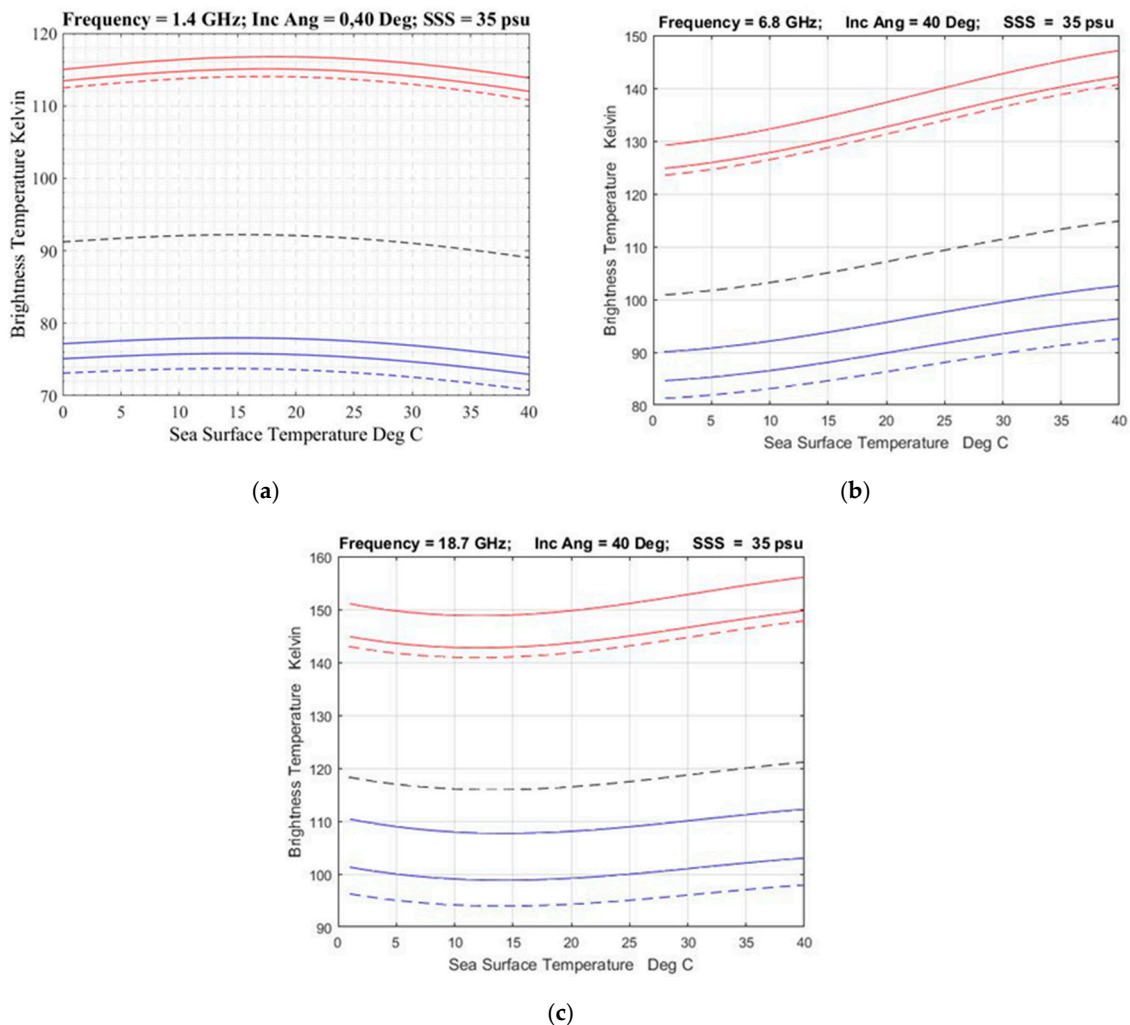


Figure 10. Brightness temperature vs. SST for constant wind speed at: (a) 1.4 GHz; (b) 6.8 GHz; (c) 18.7 GHz. The dashed curves are for 0 m/s. Black dashed is at nadir, red is vertical polarization and blue is horizontal polarization at 40° incidence angle. The solid curves are for WS = 7 and 14 m/s.

3.3.3. Sensitivity of TB to Changes in WS: dTB/dWS

The sensitivity, dTB/dWS , is approximately the change between the level curves in Figure 8 at fixed SST divided by the change in wind speed. From Figure 8 one can see qualitatively that the sensitivity increases with wind speed but not uniformly because the spacing is different at very low wind speed (below 2 m/s) and changes again above about 8 m/s. It also is clear from Figure 10 that the spacing depends on polarization, being noticeably larger at horizontal polarization.

Figure 11 reports quantitative values of dTB/dWS computed from the empirical model of Meissner and Wentz [22] for 6.8 GHz (Figure 11b) and 18.7 GHz (Figure 11c) and the model of Yin et al. [29] for 1.4 GHz. The figure reports the sensitivity of brightness temperature to wind speed plotted on the vertical axis as a function of wind speed on the horizontal axis. In each case, SST = 20 °C and SSS = 35 psu which are close to the average values for the open ocean. The dashed curves are for horizontal polarization and solid curves are for vertical polarization and examples are given for incidence angles of 20° (blue) and 40° (red). For wind speed in the range of about 5 m/s < WS < 15 m/s, the sensitivity increases almost linearly with WS at these frequencies and the shape of the curve is almost independent of polarization. However, the value of sensitivity depends on polarization, being larger for horizontal polarization at all three frequencies. The sensitivity also increases with frequency and for a given polarization and incidence angle, the sensitivity is greater the higher the frequency.

At a given frequency, the sensitivity increases with incidence angle at horizontal polarization and decreases with incidence angle at vertical polarization. A similar behavior was observed at L-band in the Aquarius data (e.g., see. Figure 2 in [31]).

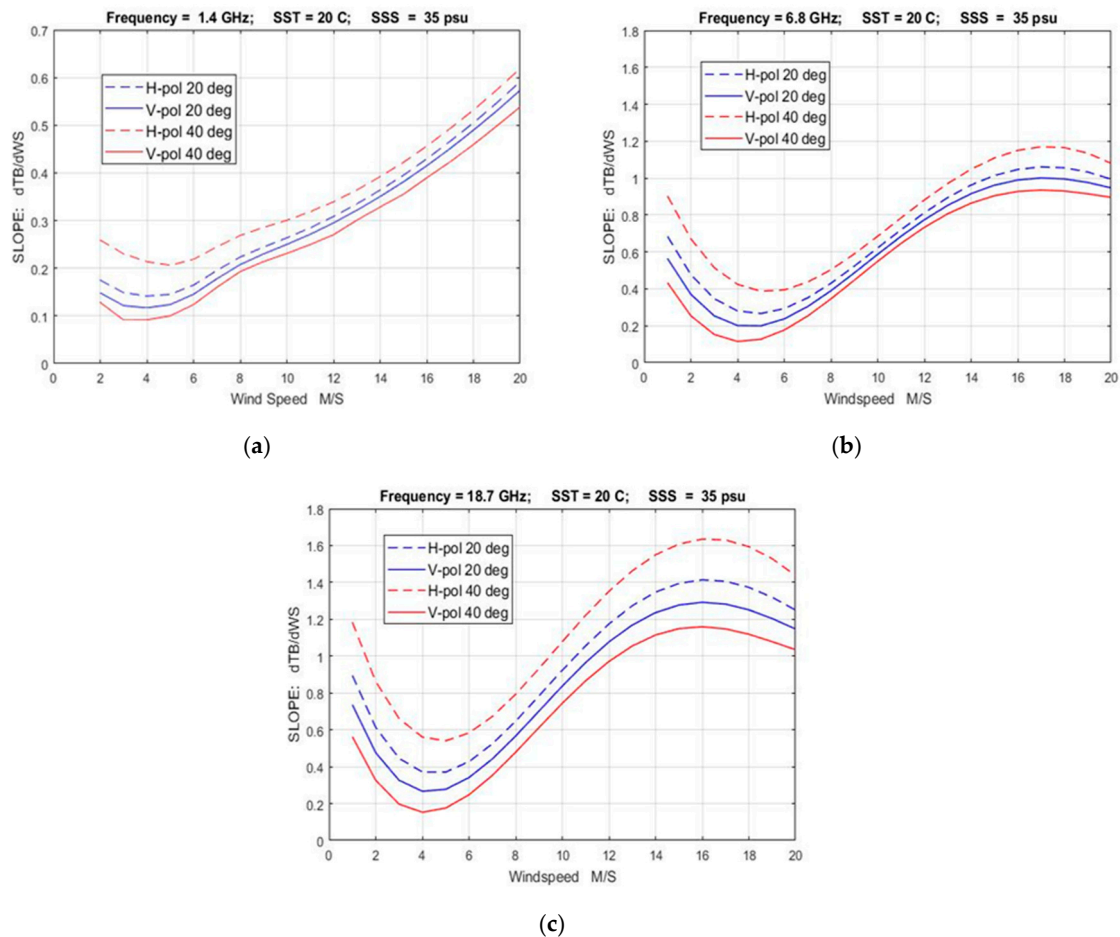


Figure 11. Sensitivity, dTB/dWS, of brightness temperature to a change in wind speed for incidence angles of 20° and 40° and SST = 20 °C; SSS = 35 psu: (a) 1.4 GHz; (b) 6.8 GHz; (c) 18.7 GHz.

Figure 11 indicates that for $WS < 4$ m/s the sensitivity, dTB/dWS, stops decreasing and for lower wind speed begins to increase as the wind speed decreases. Evidence of this can be seen in Figure 8 where the distance between the level curves at $WS = 0$ m/s and $WS = 2$ m/s (the lowest two curves) is larger than distance between the level curves for the next steps in WS. This is independent of frequency and is a characteristic of theory (e.g., at 1.4 GHz from the model of Yin et al. [29]) and also from the empirical data at 6.8 GHz and 18.7 GHz from Meissner and Wentz [22]. On the other hand, at high wind speed, Figure 11 shows that for $WS > 15$ m/s, the sensitivity at 6.8 GHz and 18.7 GHz begins to level out and decrease, but this is not true at 1.4 GHz where the sensitivity continues to increase. The Yin et al. model [29] suggests that this may be an effect of foam. Foam increases with wind speed in the model, and it may be that at $WS > 15$ m/s the higher frequencies are beginning to show the effect of saturation due to attenuation by foam which has not yet become significant at 1.4 GHz because of its much longer wavelength.

3.3.4. Frequency Dependence of Sensitivity: dTB/dWS

The calculations of the sensitivity, dTB/dWS, at selected frequencies, such as shown in Figure 11, have been collected to produce a summary showing how the sensitivity varies with frequency. This is reported in Figure 12 which shows dTB/dWS as a function of frequency for a wind speed of 7 m/s

and an incidence angle of 40° . This example is for $SST = 20^\circ\text{C}$ and $SSS = 35$ psu and covers the frequency range 500 MHz to 85.5 GHz. The solid curves (magenta for vertical polarization and orange for horizontal polarization) are smooth fits to the “data” points (circles and stars). The data above 5 GHz was taken from the Meissner-Wentz empirical model [22] which provides fits to the data at five frequencies (6.8, 10.7, 18.7, 37.0 and 85.5 GHz), and the data at frequencies below 5 GHz was computed from the Yin et al. model [29]. The Yin et al. model uses a two-scale model for the surface with the Durden and Vesecky [32] wave spectrum multiplied by 1.25. It includes a foam model that results in a reduced foam fraction compared to higher frequencies to account for the larger penetration depth at L-band. The foam model has been fitted to the radiometric observations of SMOS at multiple incidence angles [29]. It shows a good agreement with the Aquarius (empirical) model function for the dependence of TB on wind speed and the empirical model function developed for SMAP [29–31]. It is worth noting that the data from both theory and empirical models seem to fit well to a single smooth curve (the solid curves in Figure 12). The only noticeable outlier is the point for vertical polarization at 37 GHz.

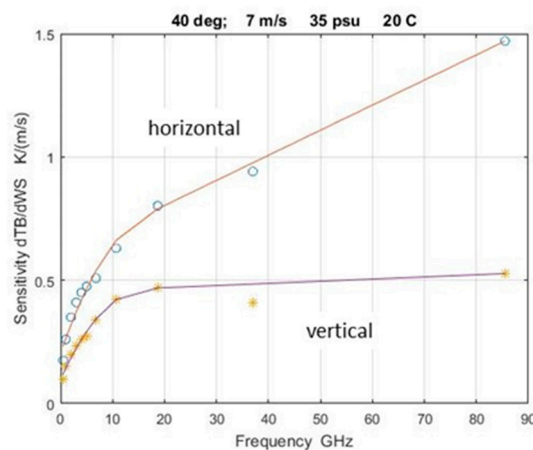


Figure 12. Sensitivity of brightness temperature to wind speed, dTB/dWS , as a function of frequency: Incidence angle = 40° ; $WS = 7$ m/s; $SST = 20^\circ\text{C}$; $SSS = 35$ psu.

Figure 12 is for a single wind speed (7 m/s) and single incidence angle (40°). On the basis of the discussion above, the curves of sensitivity at vertical and horizontal polarization will move toward each other at smaller incidence angle (e.g., Figures 10 and 11) converging to a single curve at nadir. On the basis of the examples shown in Figure 11, one would expect the change to scale proportionately with wind speed for at least $WS < 15$ m/s. Based on the parallel nature of the curves in Figure 8, one would expect only minor changes with SST, and at frequencies above a few GHz one would expect no change with SSS (Figure 4).

4. Discussion

The characteristics of the sensitivities, defined in Equation (1), needed to understand how brightness temperature, TB, changes with salinity, water temperature and wind speed are summarized in Figures 13 and 14. Figure 13 is a composite showing the sensitivity of brightness temperature to changes in sea surface salinity ($dTB/dSSS$, black), to changes in sea surface temperature ($dTB/dSST$, red) and to changes in wind speed (dTB/dWS , blue) plotted together on the same scale. This example is for an incidence angle of 40° ; Figure 13a shows the results for horizontal polarization, and Figure 13b gives the results for vertical polarization. The figures also include an indication of the attenuation by the atmosphere (dashed line) over this frequency range (see Appendix C for a description of the model used).

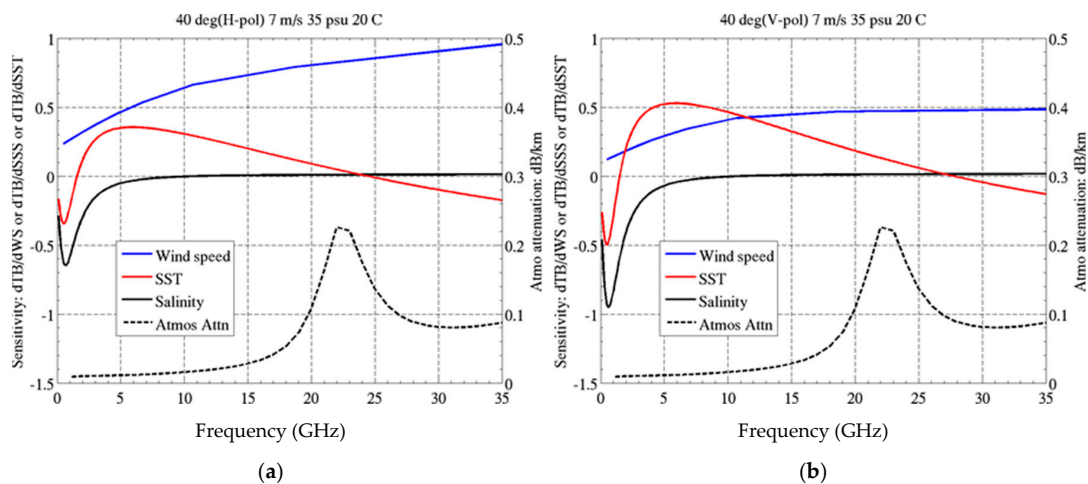


Figure 13. Sensitivity of brightness temperature to WS (blue), SST (red) and SSS (black) for 40° incidence, WS = 7 m/s, SSS = 35 psu and SST = 20 °C. The figures also indicate attenuation due to the atmosphere (dashed line). For attenuation, the vertical axis is attenuation in dB per km at nadir. (a) Horizontal polarization; (b) Vertical polarization.

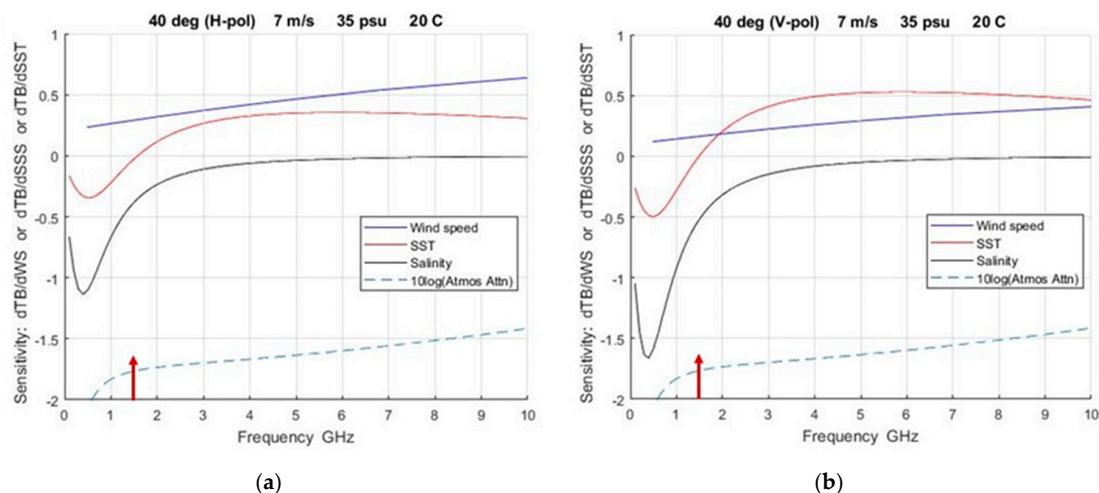


Figure 14. Expanded view of sensitivities shown in Figure 13 with more frequency resolution in the range relevant to remove sensing of SSS: (a) Horizontal polarization; (b) Vertical polarization. The arrow indicates 1.4 GHz.

The sensitivities in Figure 13 are plotted on a common scale for the three parameters (i.e., the range on the vertical scale represents sensitivity to SSS, SST or WS depending on the parameter). For example, at 5 GHz and horizontal polarization, $dTB/dSSS \approx 0$ K/psu (solid black curve), $dTB/dSST \approx 0.4$ K/°C (red curve) and $dTB/dWS \approx 0.5$ K/(m/s) (blue curve). Using the same data plotted with expanded scale (Figure 14), it can be seen that the change in TB due to a change in SSS is negligible at 5 GHz, but at 1 GHz an increase in SSS of 1 psu results in a decrease in TB on the order of 0.6 K at horizontal polarization and 0.9 K at vertical polarization. On the other hand, the sensitivity to changes in SST at 5 GHz is on the order of 0.5 K/°C at vertical polarization, meaning that a change of 1 °C results in a change of TB of 0.5 K. Of course, whether these changes are significant or not depends on the science requirements for the particular parameter: For example, a typical requirement for remote sensing of SSS from space is 0.2 psu whereas the requirement for SST to meet this goal in the retrieval is on the order of 0.5 °C.

The atmospheric attenuation (dashed line) is assumed to be independent of polarization and the value reported in Figure 13 is the attenuation/km at the bottom of the atmosphere for an atmosphere

with 60% relative humidity and a surface temperature of 20 °C. The peak in attenuation near 22 GHz is due to water vapor. The attenuation is small at frequencies important for remote sensing of salinity, although significant enough to be included in the retrieval [16]. Additional details are provided in Appendix C.

Figure 14 shows the data in Figure 13 with expanded frequency scale for frequency below 10 GHz, which are more representative of those likely to be used for remote sensing of salinity. It can be seen from Figure 14 that using frequencies lower than the 1.413 GHz currently employed for remote sensing from space (i.e., by SMOS, Aquarius and SMAP) will improve sensitivity to salinity (black curve) and decrease sensitivity to wind speed (blue curve). However, there is also a negative consequence because such a change increases the sensitivity to SST (red curve). The protected band at 1.413 GHz (arrow) is almost ideal for its small sensitivity to changes in SST. Thus, moving to a lower frequency to improve sensitivity to SSS will also increase the sensitivity to SST, and a higher sensitivity to SST means a requirement for a more accurate value of SST in the retrieval (see Equation (1)). To counter this need for more accuracy in SST, a frequency more sensitive to SST might be added. For example, something in the vicinity of 3 GHz would provide good sensitivity to SST, independence of SSS and not a large increase in the effect of wind speed (blue). Studies have been reported of sensor designs to accommodate such changes [3–5] but as mentioned above, the challenges of such instruments are significant, including the need for bigger antennas at lower frequencies to mitigate the loss in spatial resolution and the presence of radio frequency interference (RFI) in shared and/or unprotected bands (Appendix D). Hopefully, data such as presented in Figures 13 and 14 will help in making the trades necessary in the design of a future instrument.

5. Conclusions

Figures 13 and 14 summarize the detailed analysis in Section 3 of the relative role of sea surface salinity (SSS), sea surface temperature and wind speed in determining the change in brightness temperature observed from the ocean surface. Understanding how the brightness temperature responds to each of these parameters is important for evaluating the potential for adding new frequencies to improve remote sensing of sea surface salinity from space and especially to improve accuracy in cold water, which is of increasing importance in the era of climate change. Figures 13 and 14 provide a guide to help understand the algorithm trades involved in choosing new and/or alternate frequencies for remote sensing in the future.

Author Contributions: Both authors D.M.L.V. and E.P.D. have contributed equally to all aspects of this study and the writing of this manuscript. All authors have read and agreed to the published version of the manuscript.

Funding: This research was funded by the National Aeronautics and Space Administration, grant number 80NSSC18K0384.

Conflicts of Interest: The authors declare no conflict of interest. The funders had no role in the design of the study; in the collection, analyses, or interpretation of data; in the writing of the manuscript, or in the decision to publish the results.

Appendix A. Model Functions for the Dielectric Constant of Sea Water

The model functions, $\epsilon(S, T, f)$, for the dielectric constant of sea water in most common use for remote sensing of the ocean surface employ a Debye resonance term for the polarizability of the water molecule plus a salinity dependent term for the conductivity [19,33]. See [23] for a history. Examples are the model by Klein and Swift [19] and a version with resonance at two frequencies by Meissner and Wentz [21,34]. Recently, a model specifically developed for application at 1.413 GHz and remote sensing of salinity, has been reported by the team at the George Washington University [23,24]. The differences can be important at 1.413 GHz for remote sensing of salinity (e.g., Figure 16 in [9]) where the requirements are on the order of 0.1 K to meet a science requirement of 0.2 psu. However, in terms of trends, the model functions are very similar, especially in the frequency range of interest in this manuscript.

This is illustrated in Figure A1 which shows the brightness temperature for an ideal ocean surface (i.e., flat and homogeneous) at 40° incidence for the three contemporary model functions: KS (Klein-Swift [19]); MW (Meissner and Wentz, [34]); and GW (Zhou et al., [35]). The GW model function was originally in the form of a polynomial in salinity and temperature [23] because it was intended for use only at 1.4 GHz. Recently, additional measurements were reported [36] and the data was fitted to the same Debye model function used by Klein and Swift [35]. This latest form is the version of GW shown in Figure A1.

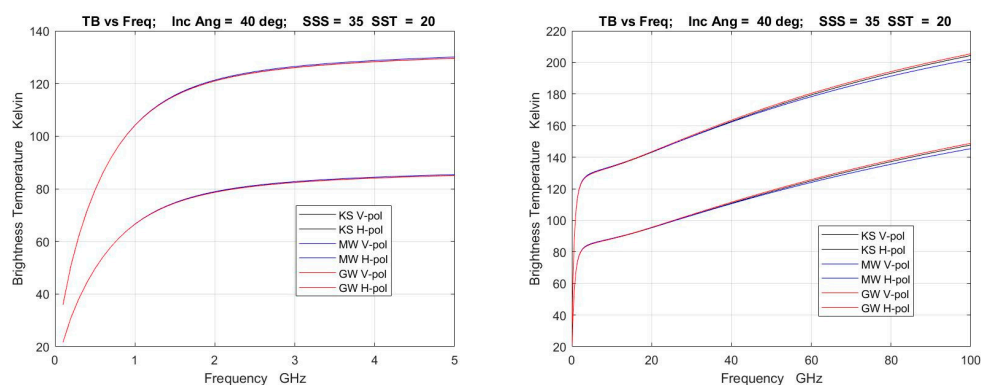


Figure A1. Comparison of the brightness temperature as a function of frequency for three model functions for the dielectric constant of sea water: KS = Klein-Swift [19]; MW = Meissner-Wentz [34]; GW = Zhou et al. [35]. The two figures are the same with expanded scale on the left to show details near 1.4 GHz where salinity is currently measured.

On the scale shown in Figure A1, the TB predicted by the three model functions only differs noticeably at very high frequencies (greater than about 50 GHz; Figure A1 right). This is somewhat surprising since the GW model is based only on data at one frequency, 1.413 GHz, and the KS model was based on data only at 1.4 GHz and 2.65 GHz. Only the MW model was tuned to apply at higher frequencies [21,34]. However, see [23,24] for a comparison at 1.4 GHz where there are small differences (order of 1 K) as a function of temperature and salinity. These differences can be important in the context of the retrieval of SSS [9] where the level of desired accuracy is on the order of 0.1 K (i.e., 0.2 psu). However, in terms of trends such as sensitivity to salinity presented here, these differences are small. This is illustrated in Figure A2 which shows the sensitivity, $dTB/dSSS$, at nadir computed using the three model functions. At the level of resolution reported here, the curves are almost indistinguishable below a few GHz.

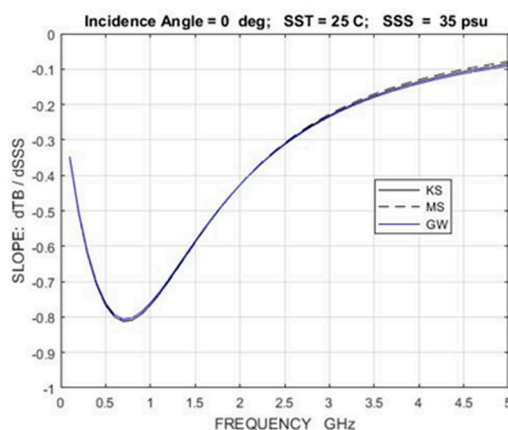


Figure A2. Comparison of the sensitivity, $dTB/dSSS$, computed with the three model functions for the dielectric constant of sea water: KS = Klein-Swift [19]; MW = Meissner-Wentz [34]; GW = Zhou et al. [35]. These examples are for SST = 25 °C and SSS = 35 psu and no wind (flat surface).

Appendix B. Dependence on Salinity

Appendix B.1. $dTB/dSST$

At low frequency (e.g., below 10 GHz) the sensitivity of TB to changes in SST shown in Figure 7 depends on salinity. However, the change in sensitivity is small at values of SSS representative of the open ocean (e.g., $32 < SSS < 36$ psu). This is illustrated in Figure A3 which shows the sensitivity, $dTB/dSST$, as a function of salinity in this range for a fixed SST. For frequencies higher than 10 GHz, the dependence on SSS is negligible.

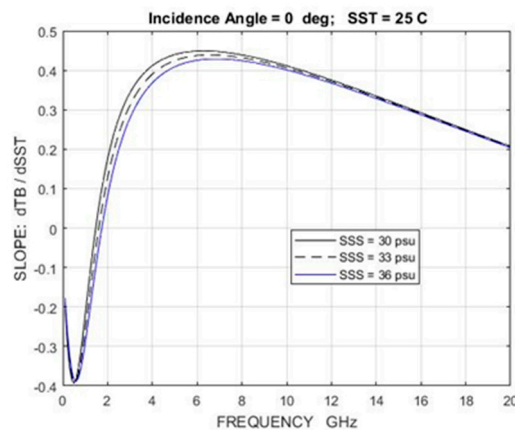


Figure A3. Dependence on salinity of the sensitivity of brightness temperature to changes in temperature, $dTB/dSST$, for salinity found in the open ocean. This example is for nadir, $SST = 25$ °C and a flat surface ($WS = 0$ m/s) using the Klein-Swift model function [19]. Top curve: 30 psu; middle curve (dashed): 33 psu; bottom curve: 36 psu.

Appendix B.2. $dTB/dSSS$

The sensitivity to salinity itself, $dTB/dSSS$, also depends on salinity but the dependence, at SST and SSS typical of the open ocean, is significant only near the peak sensitivity. This is illustrated in Figure A4 which shows $dTB/dSSS$ for $30 < SSS < 36$ psu and $SST = 25$ °C.

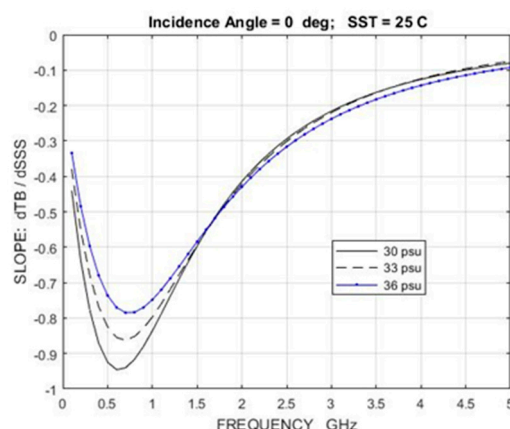


Figure A4. Dependence on salinity of the sensitivity of brightness temperature to changes in salinity, $dTB/dSSS$, as a function of frequency. The examples are for nadir, $SST = 25$ °C and $WS = 0$ m/s and made using the Klein-Swift model function [19].

Appendix C. Atmospheric Attenuation

Although the atmosphere is relatively transparent at microwave frequencies, attenuation (and associated emission) can be important. The major contributors are water vapor and molecular Oxygen, both of which exhibit resonances in the long wavelength end of the microwave spectrum. This is illustrated in Figure A5 which shows the specific attenuation (dB/km) at the surface as a function of frequency for a representative atmosphere. The calculation was made using the MPM92 model [37,38] with updated resonance line parameters from [39]. The blue dashed curve is for a dry atmosphere (no water vapor), the green dashed curve is the contribution of water vapor, and the red curve is the total attenuation. In Figure A5a the first (smaller) peak near 24 GHz is a resonance due to water vapor and the second, larger peak near 60 GHz is due to Oxygen. Figure A5b shows the same data expanded to show detail in the range of frequencies important for remote sensing of the ocean surface. The values shown in Figure A5 are for nadir (looking straight up/down). To a reasonable first approximation, values at nonzero incidence angles can be obtained by dividing by $\cos(\theta)$ for moderate values of incidence angle, θ . This example is for a surface temperature $T = 20^\circ\text{C}$ and relative humidity of 60% (8.65 g/kg of water/dry air). As the moisture content (humidity) of the atmosphere decreases, the contribution of the green curve (H_2O) decreases and the red curve (total) merges with the blue (dashed) curve.

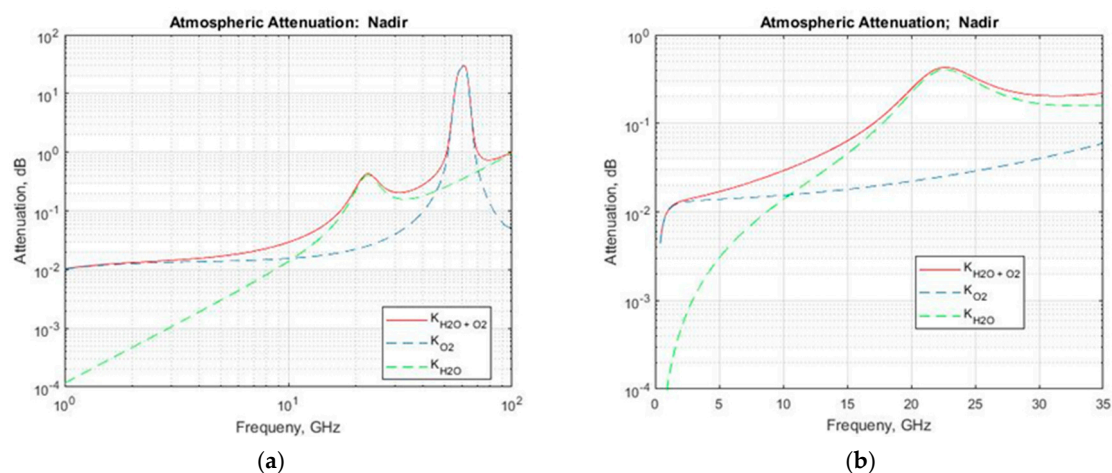


Figure A5. Specific attenuation at the surface for a standard atmosphere with $T_s = 20^\circ\text{C}$ and $\text{RH}_{20} = 60\%$. Computations using the MPM92 model [37–39]. (b) is the same as (a) but with expanded frequency scale.

Appendix D. Spectrum Management

In spectrum management language, users of the spectrum are “services” and passive remote sensing from space is the “Earth Exploration Satellite Service” (EESS). This service was established in 1971 at the World Radio Conference (WRC-71) to provide protection for passive microwave remote sensing of Earth from space [40]. Specific frequencies were assigned to EEES at WRC-79. More than 40 frequencies were allocated for passive use but most (such as the window at 1.413 GHz) coincided with allocations already in place for radio astronomy. Starting in 1994, the International Telecommunication Union, Radiocommunications Sector (ITU-R), issued recommendations for limits on interference in the passive bands (e.g., ITU-R RS.1029-2). This was updated in 2012 (ITU-R RS.2017). Table A1 reports the current recommended limits for the bands most commonly used in passive microwave remote sensing of the ocean surface (see Figure 1).

Table A1 has been included here to give an idea of the sensitive nature of passive measurements and the need for protection. The spectrum around the “windows” employed for monitoring the ocean surface is congested and several bands are only partially protected (Figure 1). Even when fully protected, as in the case of the L-band window at 1.4–1.427 GHz, the measurements encounter

man-made interference [1], [41]. In addition, remote sensing with modern instruments such as employed on Aquarius and SMAP to measure SSS are already pushing the limits in Table A1 even in protected bands. For example, the science goal of Aquarius and SMOS for measurement of ocean salinity is 0.1–0.2 psu which corresponds to a change in TB of about 0.05–0.1 K (e.g., Figure 4 in the main text).

Table A1. Protection levels for frequency bands allocated to passive microwave remote sensing.

Frequency GHz	Bandwidth MHz	Threshold		Not to Exceed % Time	Protection
		Power(dBW)	Δ TB(K)		
1.4–1.427	27	−174	0.05	0.1	Protected
6.425–7.25	200	−166	0.05	0.1	None
10.68–0.70	100	−166	0.10	0.1	Protected
18.60–18.80	200	−163	0.10	0.1	Shared
23.60–24.00	200	−166	0.05	0.01	Protected
36.00–37.00	100	−166	0.10	0.1	Shared
52.60–59.30	100	−169	0.05	0.01	Protected

Table A1 reports the recommended limits of interference expressed in terms of power and radiometric resolution, Δ TB. For an ideal total power radiometer: Δ TB = $T_{\text{sys}}/\sqrt{B\tau}$. Power and radiometric resolution are related by $P = kTB$ where k is Boltzmann’s constant and B is bandwidth. The power threshold is set at 20% of this value. The bandwidths used in the table are representative of the bandwidths actually used for remote sensing (e.g., Figure 1 in the main text). Exceptions to the thresholds are permitted but on a limited basis (“Not to Exceed” column in Table A1). The last column indicates the level of protection provided for each band.

References

1. Le Vine, D.M.; Johnson, J.T.; Piepmeier, J. RFI and Remote Sensing of the Earth from Space. In Proceedings of the Radio Frequency Interference (RFI) 2016 Conference, Socorro, NM, USA, 17–20 October 2016.
2. Le Vine, D.M.; Lagerloef, G.S.E.; Torrusio, S.E. Aquarius and Remote Sensing of Sea Surface Salinity from Space. *Proc. IEEE* **2010**, *98*, 688–703. [\[CrossRef\]](#)
3. Brown, S. A Next Generation Spaceborne Ocean State Observatory: Surface Salinity, Temperature and Ocean Winds from Equator to Pole. In Proceedings of the Global Ocean Salinity and the Water Cycle Workshop, Woods Hole, MA, USA, 22–26 May 2017.
4. Bruckner, L.; de Amici, G.; Le Vine, D.M.; Piepmeier, J. A Multi-Band Passive Radiometer for Sea Salinity, Soil Moisture and Cryosphere Studies. In Proceedings of the 2019 IEEE International Geoscience and Remote Sensing Symposium, Yokohama, Japan, 28 July–2 August 2019; pp. 8909–8912.
5. Dinnat, E.; de Amici, G.; Le Vine, D.; Piepmeier, J. Next generation spaceborne instrument for monitoring ocean salinity with application to the coastal zone and cryosphere. In Proceedings of the 15th Specialist Meeting on Microwave Radiometry and Remote Sensing of the Environment, Cambridge, MA, USA, 27–30 March 2018.
6. Kerr, Y.H.; Waldteufel, P.; Wigneron, J.-P.; Delwart, S.; Cabot, F.; Boutin, J.; Escorihuela, M.-J.; Font, J.; Reul, N.; Gruhier, C.; et al. The SMOS Mission: New Tool for Monitoring Key Elements of the Global Water Cycle. *Proc. IEEE* **2010**, *98*, 666–687. [\[CrossRef\]](#)
7. Le Vine, D.M.; Lagerloef, G.S.E.; Colomb, F.R.; Yueh, S.H.; Pellerano, F.A. Aquarius: An instrument to monitor sea surface salinity from space. *IEEE Trans. Geosci. Remote Sens.* **2007**, *45*, 2040–2050. [\[CrossRef\]](#)
8. Entekhabi, D.; Njoku, E.G.; O’Neill, P.E.; Kellogg, K.H.; Crow, W.T.; Edelstein, W.N.; Entin, J.K.; Goodman, S.D.; Jackson, T.J.; Johnson, J.; et al. The soil moisture active passive (SMAP) mission. *Proc. IEEE* **2010**, *98*, 704–716. [\[CrossRef\]](#)
9. Dinnat, E.P.; Le Vine, D.M.; Boutin, J.; Meissner, T.; Lagerloef, G. Remote Sensing of Sea Surface Salinity: Comparison of Satellite and In Situ Observations and Impact of Retrieval Parameters. *Remote Sens.* **2019**, *11*, 750. [\[CrossRef\]](#)

10. Le Vine, D.M.; Dinnat, E.P.; Meissner, T.; Wentz, F.J.; Kao, H.-Y.; Lagerloef, G.; Lee, T. Status of Aquarius and Salinity Continuity. *Remote Sens.* **2018**, *10*, 1585. [\[CrossRef\]](#)
11. Kao, H.; Lagerloef, G.; Lee, T.; Melnichenko, O.; Meissner, T.; Hacker, P. Assessment of Aquarius Sea Surface Salinity. *Remote Sens.* **2018**, *10*, 1341. [\[CrossRef\]](#)
12. Tang, W.; Yueh, S.; Yang, D.; Fore, A.; Hayashi, A.; Lee, T.; Fournier, S.; Holt, B. The Potential and Challenges of Using Soil Moisture Active Passive (SMAP) Sea Surface Salinity to Monitor Arctic Ocean Freshwater Changes. *Remote Sens.* **2018**, *10*, 869. [\[CrossRef\]](#)
13. Garcia-Eidell, C.; Comiso, J.C.; Dinnat, E.; Brucker, L. Satellite observed salinity distributions at high latitudes in the Northern Hemisphere: A comparison of four products. *J. Geophys. Res. Oceans* **2017**, *122*, 7717–7736. [\[CrossRef\]](#)
14. Garcia-Eidell, C.; Comiso, J.C.; Dinnat, E.; Brucker, L. Sea surface salinity distribution in the Southern Ocean as observed from space. *J. Geophys. Res. Oceans* **2018**. [\[CrossRef\]](#)
15. Rahmstorf, S. Thermohaline Ocean Circulation. Available online: https://courses.seas.harvard.edu/climate/eli/Courses/EPS281r/Sources/Thermohaline--circulation/1--Rahmstorf_EQS_2006.pdf (accessed on 23 April 2020).
16. Duncan, B.N.; Ott, L.E.; Abshire, J.B.; Brucker, L.; Carroll, M.L.; Carton, J.; Comiso, J.C.; Dinnat, E.P.; Forbes, B.C.; Gonsamo, A.; et al. Space-based Observations for Understanding Changes in the Arctic–Boreal Zone. *Rev. Geophys.* **2019**, *58*, e2019RG000652. [\[CrossRef\]](#)
17. Meissner, T.; Wentz, F.; Le Vine, D.M. The salinity retrieval algorithms for NASA Aquarius version 5 and SMAP Version 3 releases. *Remote Sens.* **2018**, *10*, 1121. [\[CrossRef\]](#)
18. Wilheit, T.T. A model for the microwave emissivity of the ocean's surface as a function of wind speed. *IEEE Trans. Geosci. Electron.* **1979**, *17*, 244–249. [\[CrossRef\]](#)
19. Klein, L.; Swift, C. An improved model for the dielectric constant of seawater at microwave frequencies. *IEEE Trans. Antennas Propag.* **1977**, *25*, 104–111. [\[CrossRef\]](#)
20. Peake, W. Interaction of electromagnetic waves with some natural surfaces. *IRE Trans. Antennas Propag.* **1959**, *7*, 324–329. [\[CrossRef\]](#)
21. Meissner, T.; Wentz, F.J. The complex dielectric constant of pure and sea water from microwave satellite observations. *IEEE Trans. Geosci. Remote Sens.* **2004**, *42*, 1836–1849. [\[CrossRef\]](#)
22. Meissner, T.; Wentz, F.J. The emissivity of the ocean surface between 6 and 90 GHz over a large range of wind speeds and earth incident angles. *IEEE Trans. Geosci. Remote Sens.* **2012**, *50*, 3004–3026. [\[CrossRef\]](#)
23. Zhou, Y.; Lang, R.H.; Dinnat, E.P.; Le Vine, D.M. L-Band Model Function of the Dielectric Constant of Sea Water. *IEEE Trans. Geosci. Remote Sens.* **2017**, *55*, 6964–6974. [\[CrossRef\]](#)
24. Lang, R.; Zhou, Y.; Utku, C.; Le Vine, D.M. Accurate measurements of the dielectric constant of seawater at L band. *Radio Sci.* **2016**, *51*, 2–24. [\[CrossRef\]](#)
25. Roemmich, D. On the design and Implementation of Argo—An initial Plan for a Global Array of Profiling Floats. Available online: <http://www.argo.ucsd.edu/argo--design.pdf> (accessed on 23 April 2020).
26. Hollinger, J.P. Passive microwave measurements of sea surface roughness. *IEEE Trans. Geosci. Electron.* **1971**, *9*, 165–169. [\[CrossRef\]](#)
27. Camps, A.; Font, J.; Vall-llossera, M.; Gabarró, C.; Corbella, I.; Duffo, N.; Torres, F.; Blanch, S.; Aguias, A.; Villarino, R.; et al. The WISE 2000 and 2001 campaigns in support of the SMOS mission: Sea surface L-band brightness temperature observations and their application to multiangular salinity retrieval. *IEEE Trans. Geosci. Remote Sens.* **2004**, *42*, 804–824. [\[CrossRef\]](#)
28. Yueh, S.H.; Dinardo, S.J.; Fore, A.G.; Li, F.K. Passive and active L-band microwave observations and modeling of ocean surface winds. *IEEE Trans. Geosci. Remote Sens.* **2010**, *48*, 3087–3100. [\[CrossRef\]](#)
29. Yin, X.; Boutin, J.; Dinnat, E.; Song, Q.; Martin, A. Roughness and foam signature on SMOS–MIRAS brightness temperatures: A semi-theoretical approach. *Remote Sens. Environ.* **2016**, *180*, 221–233. [\[CrossRef\]](#)
30. Dinnat, E.P.; Burgin, M.; Colliander, S.; Chae, C.; Cosh, M.; Gao, Y. Intercalibration of Low Frequency Brightness Temperature Measurements for Long-Term Soil Moisture Record. In Proceedings of the IEEE International Geoscience and Remote Sensing Symposium (IGARSS), Valencia, Spain, 22–27 July 2018; pp. 88–91.
31. Yueh, S.H.; Tang, W.; Fore, A.G.; Neumann, G.; Hayashi, A.; Freedman, A.; Chaubell, J.; Lagerloef, G.S.E. L-Band Passive and Active Microwave Geophysical Model Functions of Ocean Surface Winds and Applications to Aquarius Retrieval. *IEEE Trans. Geosci. Remote Sens.* **2013**, *51*, 4619. [\[CrossRef\]](#)

32. Durden, S.L.; Vesecky, J.F. A physical radar cross-section model for a wind-driven sea with swell. *IEEE J. Ocean. Eng.* **1985**, *10*, 445–451. [[CrossRef](#)]
33. Stogryn, A. Equations for calculating the dielectric constant of saline water. *IEEE Trans. Microw. Theory Tech.* **1971**, *19*, 733–736. [[CrossRef](#)]
34. Meissner, T.; Wentz, F.; Ricciardulli, L. The emission and scattering of L-band microwave radiation from rough ocean surfaces and wind speed measurements from Aquarius. *J. Geophys. Res. Oceans* **2014**, *119*. [[CrossRef](#)]
35. Zhou, Y.; Lang, R.H.; Dinnat, E.P.; Le Vine, D.M. L-Band Seawater Debye Model Development and Its Application to Salinity Retrieval from Aquarius Satellite Data. In preparation.
36. Zhou, Y.; Lang, R.H.; Dinnat, E.P.; Le Vine, D.M. L-Band Seawater Dielectric Constant Model Function Based on Improved Measurement Data Set. In Proceedings of the International Geoscience and Remote Sensing Symposium, Yokohama, Japan, 28 July–2 August 2019.
37. Liebe, H.J. An updated model for millimeter wave propagation in moist air. *Radio Sci.* **1985**, *20*, 1069–1089. [[CrossRef](#)]
38. Liebe, H.J.; Rosenkranz, P.W.; Hufford, G.A. Atmospheric 60-GHz Oxygen Spectrum: New Laboratory Measurements and Line Parameters. *J. Quant. Spectrosc. Radiat. Transf.* **1992**, *48*, 629–643. [[CrossRef](#)]
39. Rosenkranz, P.W. Water Vapor Microwave Continuum Absorption: A Comparison of Measurements and Models. *Radio Sci.* **1998**, *33*, 919–928. [[CrossRef](#)]
40. National Academies of Science, Engineering and Medicine. *Handbook of Frequency Allocations and Spectrum Protection for Scientific Uses*, 2nd ed.; National Academies Press: Washington, DC, USA, 2015.
41. Le Vine, D.M.; de Mattheis, P. Aquarius Active/Passive RFI Environment at L-Band. *IEEE Geosci. Remote Sens. Lett.* **2014**, *11*, 1747–1751. [[CrossRef](#)]



© 2020 by the authors. Licensee MDPI, Basel, Switzerland. This article is an open access article distributed under the terms and conditions of the Creative Commons Attribution (CC BY) license (<http://creativecommons.org/licenses/by/4.0/>).